Bulletin of Volcanology (2024) 86:87
https://doi.org/10.1007/s00445-024-01772-2

RESEARCH ARTICLE

Magma recharge at Manam volcano, Papua New Guinea, identified through thermal and SO_2 satellite remote sensing of open-vent emissions

Adam S. Cotterill[1] · Emma J. Nicholson[1,2] · Catherine S. L. Hayer[3,4] · Christopher R. J. Kilburn[1]

Received: 26 January 2024 / Accepted: 11 September 2024

Abstract

Manam is one of the most frequently active volcanoes in Papua New Guinea and is a top contributor to global volcanic volatile emissions due to its persistent open-vent degassing. Here, we present a multi-year time series (2018–2021) of thermal and SO_2 emissions for Manam from satellite remote sensing, which we interpret in the context of open-vent feedback between magma supply, reservoir pressure, and outgassing. We classify the time series into four phases based on the varying SO_2 flux and observe a transient, yet substantial, increase in time-averaged SO_2 flux from background levels of ~ 0.6 to ~ 4.72 kt day^{-1} between March and July 2019. We also identify a transition from temporally coupled to decoupled gas and thermal emissions during this period which we explain in the context of a magma recharge event that supplied new, volatile-rich magma to the shallow plumbing system beneath Manam. We infer that the arrival of this recharge magma triggered the series of eruptions between August 2018 and March 2019. These explosive events collectively removed 0.18 km^3 of degassed residual magma and signalled the onset of a renewed period of unrest that ultimately culminated in a major eruption on 28 June 2019. We quantify the magnitude of "excess" degassing at Manam after the removal of the inferred residual magma. SO_2 emissions reveal that ~ 0.18 km^3 of magma was supplied, but only ~ 0.08 km^3 was erupted between April 2019 and December 2021. We highlight how multi-parameter remote sensing observations over months to years enable the interpretation of open-vent processes that may be missed by short-duration campaign measurements.

Keywords Magma recharge · Open-vent · Remote sensing · Thermal anomalies · SO_2 degassing

Introduction

Open-vent volcanism is sustained by the ascent and degassing of magma at shallow depths (Kazahaya et al. 1994; Harris et al. 1999; Shinohara 2008; Johnson et al. 2010; Palma et al. 2011), with variable contributions from both conduit convection and deep-derived segregated fluids that transfer both heat and volatiles to shallow reservoirs (Caricchi et al. 2018; Edmonds et al. 2022a). Open-vent systems exhibit a spectrum of eruptive styles: silica-rich magmas can form lava domes that may trigger Vulcanian eruptions if collapse occurs (Stefan 1879; Robin et al. 1991; Wooster and Kaneko 1998; Calder et al. 1999; Young et al. 2003; James and Varley 2012; Mueller et al. 2013; Girina 2013; Flower and Carn 2015; Shevchenko et al. 2020), while more mafic magmas support open conduit conditions allowing increased mobility of both melt and volatiles and, in rare cases, maintain lava lakes over years to decades.

A common characteristic of open-vent volcanoes is persistent degassing (Rose et al. 2013; Vergniolle and Métrich 2021), where the volume of magma required to supply the observed volatile flux exceeds that erupted; this is referred to as the "excess degassing phenomenon" (Kazahaya et al. 1994; Shinohara 2008). The fate of this unerupted degassed magma is often explained by conduit convection (Kazahaya et al. 1994; Beckett et al. 2014; Coppola et al. 2022) or by intrusion and endogenous crustal growth (Coppola et al. 2019). In both scenarios, it remains unclear where this

Editorial responsibility: S. Vergniolle

Adam S. Cotterill
adam.cotterill.13@ucl.ac.uk

1 UCL Hazard Centre, Earth Sciences, UCL, London, UK

2 University of Waikato, Hamilton, New Zealand

3 COMET, DEES, Manchester, UK

4 Hamtec Consulting @ EUMETSAT, Darmstadt, Germany

Published online: 07 October 2024

degassed magma accumulates in the crust. Typically, SO_2 flux is used to determine the magma supply rate (Allard et al. 1994; Andres and Kasgnoc 1998; Shinohara 2008), and the magma output is often approximated using thermal emissions (Wooster and Kaneko 1998; Laiolo et al. 2018; Coppola et al. 2019, 2022). The balance between magma input and output, and changes in this budget through time, has been shown to be highly indicative of pressure and fluid dynamic perturbations within the shallow magma storage region, which can disturb open conduit processes and may ultimately lead to eruptions.

Manam (4.078° S, 145.038° E) is a frequently erupting mafic open-vent stratovolcano located ~ 19 km off the northeast coast of mainland Papua New Guinea (Fig. 1) (Palfreyman and Cooke 1976; Global Volcanism Program 2021a). Manam is situated within the Western Bismarck Arc where the arc-continent subduction has ceased. Melting of the remnant hanging slab is considered the source of volcanism based on geochemical and geophysical evidence (Abbott et al. 1994; Abbott 1995; Woodhead et al. 2010; Holm and Richards 2013). Historically, Manam has erupted magma of basaltic to basaltic andesite composition from two active craters that typically exhibit different styles of activity (Palfreyman and Cooke 1976). Main Crater hosts degassing from a broad fumarole field and is the vent from where most lava effusions originate. South Crater emits a near-constant dense gas plume and is generally the source of most explosive eruptions. The top surface of the magma column was observed at shallow depths within South Crater on 22 May 2019 (Liu et al. 2020), but the temporal persistence of this state is currently unknown aside from occasional reports of incandescence (Global Volcanism Program 2021a).

Manam is a top-ranking emitter of volcanic volatiles in a global context and is therefore an important case study with which to explore temporal variability in emissions and their relationship to subsurface processes. Satellite measurements of SO_2 using NASA's Ozone Monitoring Instrument (OMI) between 2005 and 2015 indicate an average SO_2 flux of 1480 ± 750 tonnes day^{-1} placing Manam as the 11th strongest emission source globally (Carn et al. 2017). Similarly, Manam's CO_2 flux has been estimated at 2760 ± 1570 tonnes day^{-1} making it the 10th highest emitter of volcanic CO_2 (Aiuppa et al. 2019). Direct sampling and spectroscopic measurements of Manam's plume using a Unoccupied Aerial Vehicle (UAV) in May 2019 revealed an elevated average SO_2 flux

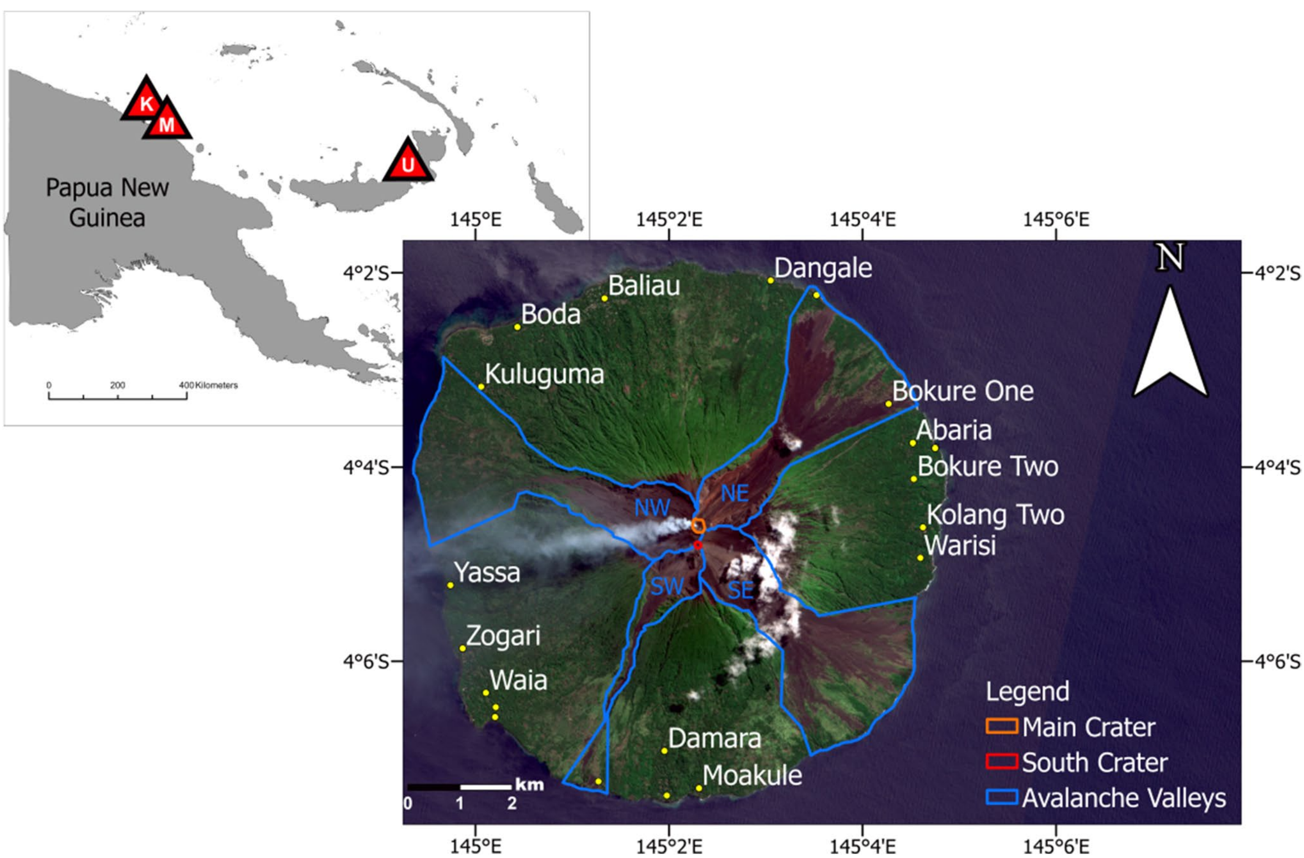

Fig. 1 Left—Map of Papua New Guinea with the locations of Manam (M), Kadovar (K), and Ulawun (U). Right—True colour image from 17 August 2020 Sentinel-2 overpass with key features of Manam Island used for Sentinel-2 imagery processing annotated

of 5150 ± [336/733] and CO_2 flux of 3760 ± [313/595] (Liu et al. 2020). These campaign-style measurements ranked Manam, albeit transiently, at 2nd and 5–7th in global inventories of volcanic SO_2 and CO_2 release, respectively.

Manam generated 29 major and 139 minor eruptions between 2000 and 2021 (Palfreyman and Cooke 1976; Global Volcanism Program 2021a). Over the same interval, frequent clusters of thermal anomaly detections were identified from satellite multispectral imagery. Following large-scale evacuations associated with the major eruptions in 2004–2005 (Johnson 2013; Connell and Lutkehaus 2016), approximately 4000 residents had returned to the island by August 2021 and experience ongoing impacts to agriculture, settlement infrastructure, and water supplies due to persistent volcanic activity (J Sukua, Pers Com., 2021).

A new phase of eruptive activity began in August 2018 after 11 months of quiescence. A series of 23 eruptions then took place until March 2019, including 5 major eruptions (i.e., eruption columns > 10 km) on 25 August 2018, 8 December 2018, 7 January 2019, 11 January 2019, and 23 January 2019. Lava effusions occurred between 27 September - 1 October 2018 and on 8 January 2019, which reached within 500 and 400 m of the coastline, respectively. The largest eruption in recent years occurred on 28 June 2019, generating an eruption column that rose to 15.2 km asl, pyroclastic density currents, and a lava flow reaching within 700 m of the coastline. During this eruption, 3775 residents evacuated temporarily, and 455 homes and agricultural gardens are reported to have been destroyed or damaged (Global Volcanism Program 2021a).

Low-viscosity open-vent systems like Manam can transition from frequent small benign eruptions to larger explosive eruptions, and the physical processes responsible for transitions are poorly understood and remain a matter of debate (Wilson 1980; Jaupart and Vergniolle 1988; Allard et al. 2005; Rose et al. 2013; Vergniolle and Métrich 2022). As such, it is difficult to identify precursory signals that are commonly difficult to identify or are entirely absent, posing challenges to local monitoring agencies responsible for providing science advice and warnings. Manam's frequent eruptions present a valuable opportunity to probe temporal variability in observable emissions and, ultimately, relate these observations to the mechanisms responsible for larger explosive eruptions at open-vent volcanoes. Further, ground-based monitoring is challenging at Manam due to the island setting, dense vegetation, steep topography, and tropical climate, and therefore key gaps remain in observational capability despite the high level of volcanic risk. Improving understanding of the relationship between satellite remote sensing observations and subsurface volcanic processes is therefore critical to augmenting future volcano monitoring at this, and other, open-vent volcanoes.

Satellite remote sensing provides regular measurements and near-global coverage of volcanic SO_2 (Theys et al. 2019) and thermal emissions (Wright et al. 2004; Coppola et al. 2016), enabling monitoring of remote or inaccessible volcanoes, such as Manam. Here, we present a multi-year time series from 2018 to 2021 of (a) SO_2 emissions derived from the European Space Agency (ESA) Sentinel-5P Tropospheric Monitoring Instrument (TROPOMI), (b) thermal anomaly detections from the National Aeronautic and Space Administration (NASA) Moderate Resolution Imaging Spectrometer (MODIS) instrument processed by the MODVOLC algorithm, and (c) surface temperature measurements in Main and South Crater using ESA's Sentinel-2 MultiSpectral Instrument (MSI). We use this multi-parameter time series to interpret magmatic processes influencing transitions in open-vent behaviour at Manam, quantify the magnitude of excess degassing and consequently the volume of unerupted degassed magma, and evaluate the time-varying contribution of Manam to global volcanic volatile emission inventories.

Methods

Sulphur dioxide (SO_2) emissions

We quantify SO_2 emissions using the TROPOMI spectrometer on board ESA's Sentinel-5P polar orbiting platform. TROPOMI has a spectral resolution of 0.25 to 0.54 nm and a spatial resolution of 3.5 × 7 km at launch (Veefkind et al. 2012) and updated to 3.5 × 5.5 km on 6 August 2019. TROPOMI observes every point on the Earth's surface at least once per day. The TROPOMI Differential Optical Absorption Spectroscopy (DOAS) retrieval algorithm calculates SO_2 Vertical Column Densities (VCDs) for each pixel within its field of view (Theys et al. 2017); VCDs are then converted to column mass (Queißer et al. 2019). The total SO_2 mass loading for a given scene is calculated by summing the column mass of SO_2 contained within each pixel above 3 times the random noise.

The TROPOMI instrumental response to SO_2 is height-dependent, and therefore, the plume altitude used is often the main source of uncertainty in SO_2 retrievals. Higher altitudes used to interpolate the SO_2 retrievals result in lower masses, and conversely, lower plumes result in higher masses. Maximum gas plume or eruption column heights, reported by RVO or Darwin Volcanic Ash Advisory Centre (VAAC), were used to represent the SO_2 plume altitude and provide conservative estimates. Visual observations from May 2019 suggest that the buoyant gas plume generally rises between a few hundred meters to ~ 1 km above the summit before dispersing laterally (Liu et al. 2020). Therefore, given Manam's summit is ~ 1800 m asl, for days without reported plume height, a maximum altitude of 3 km was used. To constrain the uncertainty related to plume height, SO_2 retrievals were calculated using minimum reported plume heights to produce a maximum SO_2 mass estimate. Where no plume height was reported, we used 2.2km asl to represent the typically observed lower gas plume altitude (Liu et al. 2020). The median difference between the minimum and maximum plume altitude SO_2 retrievals is 9% and is used here as the uncertainty on plume height. Given this uncertainty, we report SO_2 retrievals based on the maximum observed or estimated plume height throughout the remainder of this work, as they represent the best estimate of SO_2 altitude, and errors reported alongside are the TROPOMI random error.

It is important to identify other SO_2 sources that might contaminate a scene resulting in overestimation of SO_2 mass flux from Manam. Identified contamination sources include two nearby volcanoes: Kadovar (3.6069° S, 144.5878° E), which has been outgassing regularly in recent years (Plank et al. 2019, 2020; Global Volcanism Program 2021b) and Ulawun (5.0514° S, 151.3310° E), which has had five confirmed eruptions during the study period (Johnson 2013; Wood et al. 2019; Global Volcanism Program 2021c; McKee et al. 2021). TROPOMI scenes contaminated by SO_2 from external sources are identified from (a) activity reports for nearby volcanoes and (b) visual inspection of true colour Sentinel-2 images and TROPOMI VCD scenes (Fig. 2). Where possible, the measurement extent is delimited to include only the plume from Manam. If the external sources cannot be clearly separated, then the contaminated images are omitted from the time series.

Converting scene SO_2 mass into a flux requires knowledge of the residence time of SO_2 in the atmosphere. If the SO_2 lifetime exceeds 24 h, then some proportion of the SO_2 mass in a TROPOMI scene will be residual from the previous day. Uncertainties in the lifetime of SO_2 in the atmosphere make converting total scene mass to SO_2 fluxes non-trivial, especially under different atmospheric conditions (McCormick Kilbride et al. 2019). Here, the method proposed by Fioletov et al. (2015) is used where, under steady-state emissions, the flux (ΦSO_2) and SO_2 mass are related by Eq. 1:

$$\Phi SO_2 = \frac{MSO_2}{\tau} \quad (1)$$

where MSO_2 is SO_2 (tonnes), and τ is the residence time of SO_2 in the atmosphere in days. Three estimates for residence time were used in an attempt to capture the uncertainty related to this variable: 1, 2, and 3 days based on residence times used in similar studies (Beirle et al. 2014; Laiolo et al. 2018; McCormick Kilbride et al. 2019; Liu et al. 2020). The maximum atmospheric residence time for SO_2 plumes from Papua New Guinea volcanoes has previously been estimated to be ~ 18 h with typical ages being < 12 h (McCormick et al. 2012). As the timing of emissions is unknown, applying a residence time of 1 day assumes all detected SO_2 was emitted in the previous 24 h. Assuming higher residences would lead to underestimating SO_2 mass if residence times are < 1 day. Therefore, the fluxes based on a 1-day residence time are used in the discussion. Lastly, we calculate time-averaged SO_2 fluxes by fitting a first-order polynomial to the cumulative ΦSO_2 emissions (Fig. 3).

Satellite-based measurements of atmospheric SO_2 are known to be impacted by meteorological cloud cover. Meteorological clouds at a higher altitude than the SO_2 plume cause an underestimation of total column SO_2 as the cloud firstly reduces the solar radiation reaching the plume and then reduces the radiation reaching the sensor from that scattered back from the SO_2 plume itself (McCormick et al. 2013). The inverse is true for cloud altitudes lower than the SO_2 plume, as the cloud reflects more radiation back toward the satellite than would be expected from typical ground albedo which results in a higher amount of SO_2 being estimated (McCormick et al. 2013).

Correcting for the influence of the cloud on SO_2 VCD measurements is non-trivial and beyond the scope of this work. Instead, we use the cloud fraction indicator available

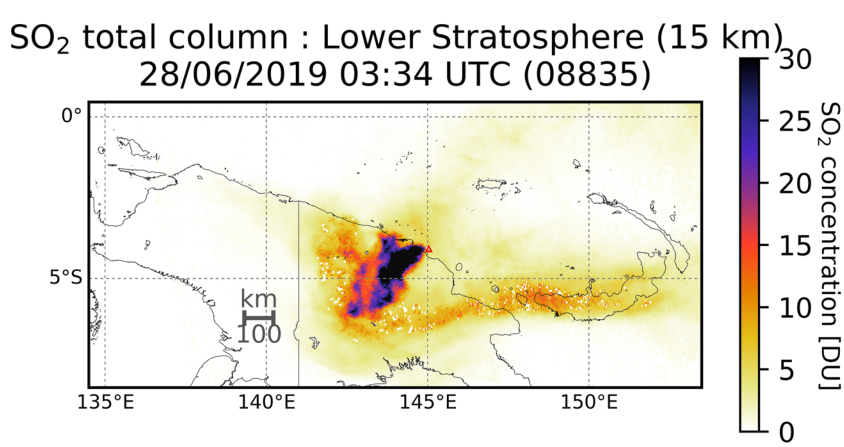

Fig. 2 TROPOMI SO_2 Vertical Column Density (VCD) interpolated at 15 km altitude over Manam on 28 June 2019 showing the SO_2 plume from the major eruption of Manam that day. This total emitted SO_2 mass was 58.3 kt on 28 June 2019. The total emitted SO_2 mass is calculated by summing all pixels within the view extent. N.B. This retrieval has a pixel resolution of 3.5 × 7 km as it was taken prior to the resolution improvement to 3.5 × 5.5 km on 6 August 2019

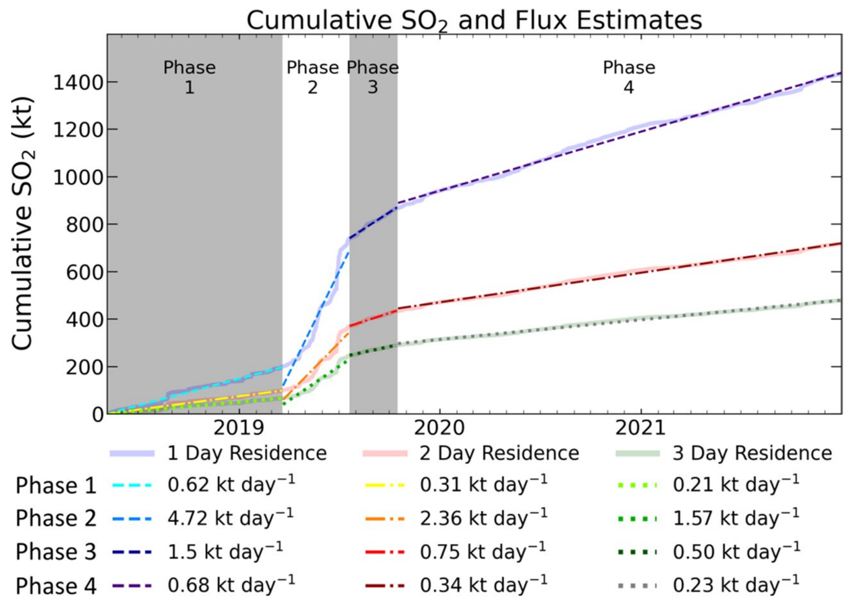

Fig. 3 Solid lines show cumulative SO_2 under 1-day (blue), 2-day (red), and 3-day (green) atmospheric residence time regimes. Each regime is divided by the 4 identified emission phases. A polynomial was fitted for each regime and phase (dashed lines), and the gradient of each line indicates the average daily flux

for every pixel in the TROPOMI SO_2 product. We take the mean cloud fraction for pixels within the target measurement area around Manam for a given overpass to produce a daily cloud fraction time series and histogram (Fig. S1). These are used as a reference to assess the possible impact of cloud cover on SO_2 retrievals from TROPOMI and consequently on the temporal trends identified.

Thermal anomalies

The MODVOLC algorithm measures the radiant heat flux, or volcanic radiative power (VRP), emitted by Manam (Wright et al. 2004; Wright 2016). MODVOLC uses Level 1B products from the MODIS multispectral instrument onboard the NASA Aqua and Terra satellites, providing a 1 km^2 pixel resolution for the infrared bands. These two satellites ensure coverage of most of Earth's surface every 1–2 days. VRP is the total heat radiated across the area of the anomaly at the time of acquisition and is expressed in W or J s^{-1} according to Eq. 2 (Coppola et al. 2013; Wooster et al. 2003; Wright et al. 2015).

$$VRP\left(\phi_e\right) = 1.89 \times A_{PIX} \times D_{PIX} \quad (2)$$

where 1.89 is a best-fit regression coefficient calculated using the MIR (Middle Infrared) method (which relates the VRP estimated by the simple power law used by MODVOLC to the expected value under the Planck function; Wooster et al. 2003), A_{PIX} is the area of the pixel, and D_{PIX} is the above-background MIR radiance of the pixel. When a hotspot is detected in more than one pixel, the total VRP is the sum of the VRP across all hotspot pixels. Thermal anomaly intensity is classified following Coppola et al. (2016): < 1 MW = Very Lo, ≥ 1MW = Low, ≥ 10MW = Moderate, ≥ 100 MW = High, ≥ 1 GW = Very High and ≥ 10 GW = Extreme.

Manam's two craters are within 1 km of each other, and so the measured VRP likely includes thermal contributions from both due to MODIS's pixel resolution. To determine the source of each anomaly, we use (a) thermal infrared (TIR) imagery from NASA's Advanced Spaceborne Thermal Emission and Reflection Radiometer (ASTER) (90 m resolution) and (b) short-wave Infrared (SWIR) (20 m resolution) and True Colour Imagery (TCI) (10 m resolution) from ESA's Sentinel-2 MSI (Fig. 4).

We use the MODIS cloud mask product to analyse the impact of cloud cover on MODVOLC thermal anomaly detections. Of particular interest is whether all "non-detections" truly represent the absence of volcanic thermal emissions or whether cloud cover is obscuring the signal from the sensor. The process and results of the cloud mask analysis can be found in Table S1.

Surface temperatures

Surface temperature within each of Manam's summit craters is derived from the Sentinel-2 MSI Level 1C product (Top of Atmosphere (TOA) Reflectance). First, TOA reflectance measured from the MSI band 11 (central wavelength of 1610 nm) is converted to radiance using Eq. 3:

$$L\lambda = \frac{Q_{cal}E_{e\lambda}(cos\theta)}{\pi\left(\frac{1}{U}\right)}/10^4 \quad (3)$$

where Q_{cal} = reflectance stored as a digital number (DN); $E_{e\lambda}$ = solar irradiance (W m^2); θ = incidence angle (°), and

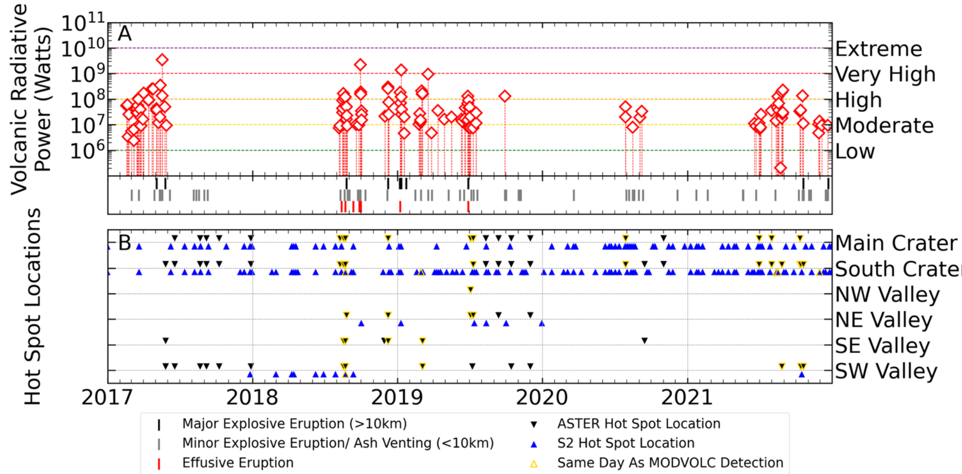

Fig. 4 **A** Time series of MODVOLC detected thermal anomalies from 2015 to 2021 at Manam and observed activity. Horizontal coloured dashed lines correspond to Volcanic Radiative Power intensities. **B** ASTER infrared imagery used to visually identify the location of anomalies. Black markers indicate an anomaly present in the key region represented by the row marker on the *y*-axis. Yellow highlighted markers represent an Aster anomaly on the same day as a MODVOLC detection

U = quantification value (converts value to TOA). $E_{e\lambda}$, θ, and U are drawn from the MSI image metadata.

Pixel Integrated Temperatures (PIT) are then calculated for each band using Eq. 4 (adapted for use with MSI imagery from Francis and Rothery 1987; Rothery et al. 1988; Harris 2013), which is derived from the Planck function (Planck 1901).

$$T = \frac{C_2}{\lambda ln\left(\left[\varepsilon\tau C_1\lambda^{-5}/10^6\pi L_\lambda\right] + 1\right)} \quad (4)$$

where L_λ = radiance (Wm^{-2} sr^{-1} μm^{-1}), $C_1 = 3.742 \times 10^{-16}$ (W m^2), $C_2 = 0.0144$ (mK), λ = wavelength (m), T = blackbody temperature (K), ε = emissivity of the radiating surface, and τ = atmospheric transmissivity. C_1 and C_2 are simplified constants representing hc^2 and hc/k, where h is Planck's constant (6.266×10^{-34} J s), c is the speed of light (2.998×10^8 m s^{-1}), and k is Boltzmann's constant (2987 μm K).

Emissivity for the basaltic andesite lava erupted at Manam (Palfreyman and Cooke 1976; McKee 1981) is estimated as 0.852 for band 11, based on basaltic andesite lavas measured for emissivity in the John Hopkins ECOSTRES Spectral Library (Meerdink et al. 2019). Atmospheric transmissivity for Manam was estimated using MODTRAN based on a cloud-free atmosphere (MODerate resolution atmospheric TRANsmission) to be 0.892 for band 11 (Berk et al. 2014) (Table S2).

Magma balance calculations

Degassing magma volume

Here, we use TROPOMI-derived SO_2 masses, estimated erupted volumes based on plume heights reported in Volcanic Ash Advisory Bulletin (Darwin VAAC), and lava flow inundation areas estimated from Sentinel-2 satellite multispectral imagery using ArcGIS to calculate the mass balance.

The volume of magma required to generate the observed SO_2 emissions is calculated using the petrological method first presented by Devine et al. (1984) and adapted into Eq. 5:

$$V = \frac{f}{c\rho\gamma\ \Delta S} \times 10^{-9} \quad (5)$$

where V = magma volume (km^3), f = measured SO_2 flux (kg d^{-1}), c = S to SO_2 conversion constant (c = 2), ρ = magma density (2640 kg m^{-3}), γ = vesicularity (expressed as melt fraction, i.e., 1 = 0% porosity, 0.7 = 30% porosity), and ΔS = degassed sulphur (ppm × 10^{-6}). Density is calculated using the method of Bottinga and Weill (1970) using bulk rock compositions from Palfreyman and Cooke (1976) and McKee (1981). The values of vesicularity and both initial and degassed melt sulphur contents are unconstrained for recent eruptive products; therefore, the vesicularity term is varied between 0 and 30%, and the total degassed sulphur is approximated as 0.2 ± 0.02 wt%, based on the upper bound of the main population of undegassed arc melt inclusion S contents (Muth and Wallace 2022) and on experimental constraints on the sulphur content at sulphide saturation for oxidation states ~ FMQ + 1 (Jugo 2009). However, we recognise that magmatic sulphur contents can be substantially higher in enriched melt inclusions (Zelenski et al. 2022) and are influenced by the composition of the mantle wedge, the addition of slab components, and whether sulphide saturation is attained either during melting or ascent.

Effusively erupted magma volume

Six lava flows were emplaced between May 2018 and December 2021, identified in satellite imagery. The area inundated by each flow was measured using ArcGIS using multispectral imagery from MSI, ASTER, and NASA's Enhanced Thematic Mapper Plus (ETM +) and Operational Land Imager (OLI) sensors aboard Landsat 7 & 8, respectively (Fig. S4).

The volume of each flow was approximated based on the average thickness of the September–October 2018 flow, which was estimated as ~ 3.5 m based on a digital elevation model (DEM) (Fig. S5) created from an Unoccupied Aerial System (DJI Mavic 2 Pro) video of Manam's Northeast Valley. A porosity of 18.8% was measured (see supplementary materials) in a lava sample from the distal portion of the 28 June 2019 lava flow and used to convert bulk volume to dense rock equivalent (DRE) (Table S3).

Explosively erupted magma volume

The volume of magma erupted during explosive events can be estimated using the relationship between eruption plume heights (H, km) and erupted volumes (V, km^3 DRE) presented by Mastin et al. (2009). This relation is empirical, based on a catalogue of 34 moderate to large explosive eruptions spanning mafic to silicic magma compositions (Eq. 6):

$$H = 25.9 + 6.64log_{10}(V) \quad (6)$$

An uncertainty of approximately one order of magnitude is associated with using Eq. 6 to calculate erupted volume from plume height (L. Mastin, Pers Com.). Here, we use Eq. 6 to calculate erupted volumes at Manam based on explosive eruption column heights reported in RVO bulletins and Darwin VAAC reports (Fig. S6).

Results

SO_2 emissions

Daily SO_2 mass loadings from Manam between 6 May 2018 and 31 December 2021 (Fig. 5e) have a mean of 1.1 kt day^{-1} and a median of 0.47 kt day^{-1}. The time series is dominated by several short-duration, high-magnitude emissions associated with explosive eruptions with 75% of daily emissions below the mean. Using a 7-day moving-average, we define four degassing phases, using a 1 kt day^{-1} threshold to distinguish Phases 1 and 4 (below threshold) from Phases 2 and 3 (above threshold), which refer to the background and elevated degassing phases, respectively. The elevated degassing phases are identified by the moving-average exceeding 1 kt day^{-1} and subsequently not dropping below this threshold for more than 8 days. The transition between Phases 2 and 3 is demarcated by a gradient change of cumulative SO_2 emissions, which occurred on 21 July 2019 (Fig. 3).

The TROPOMI meteorological cloud fraction analysis shows that over the study period, 30% of daily mean cloud fraction values were below 35%, and the average daily mean cloud fraction was 50% (Fig. S1). The cloud fraction time series in Fig. S1 shows that cloud cover is variable throughout the year, and no clear seasonality is present. Therefore, while we note that the magnitude of individual SO_2 retrievals on a given day may be impacted by cloud above or below the plume, the longer-term trends discussed in this section are not considered to be artefacts of cloud cover.

The TROPOMI meteorological cloud fraction analysis shows that over the study period, 30% of daily mean cloud fraction values were below 35%, and the average daily mean cloud fraction was 50% (Fig. S1). The cloud fraction time series in Fig. S1 reveals that cloud cover is variable throughout the year, and no clear seasonality is present. Therefore, while cloud cover will impact SO_2 detection on a given day, the trends discussed in this section are not likely to be artefacts of cloud cover.

Phase 1: 6 May 2018–21 March 2019

SO_2 emissions for Phase 1 totalled 198.8 ± 8.3 kt over 319 days, with a time-averaged SO_2 flux of 0.62 kt day^{-1}

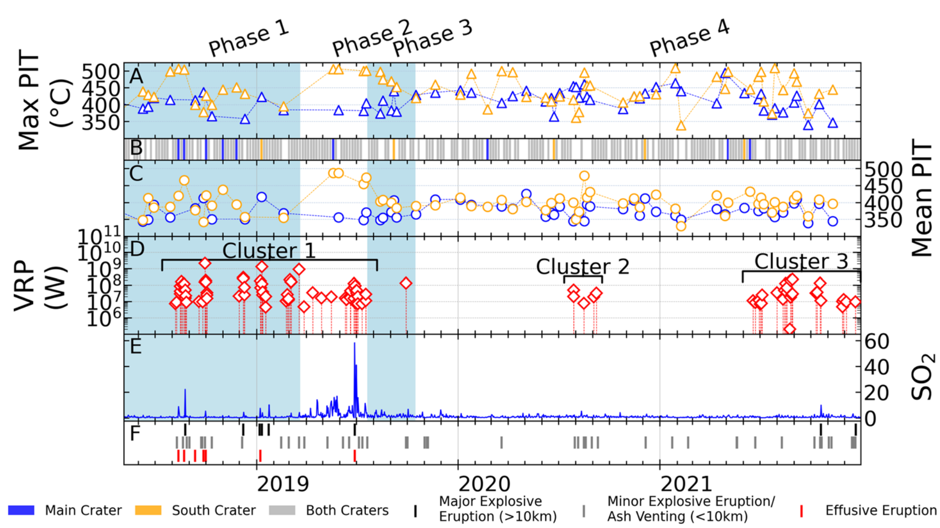

Fig. 5 Combined time series of Maximum Pixel Integrated Temperature (**A**), MSI Cloud Cover (**B**), Mean Pixel Integrated Temperature (**C**), MODVOLC thermal anomaly detection (**D**), SO_2 emissions (**E**), and activity reported by Rabaul Volcanological Observatory and Global Volcanism Program (**F**)

(Fig. 5e). After an 11-month period of eruptive quiescence, explosive eruptive activity returned on 10 August 2018, after which 13 minor explosive eruptions, 5 major explosive eruptions, and 6 effusive eruptions occurred. The daily emitted SO_2 mass exceeded 3 kt on ten occasions, all associated with explosive behaviour. The largest Phase 1 emission of 22.1 kt SO_2 is linked to explosive and effusive activity on 25 August 2018.

Phase 2: 22 March–20 July 2019

Phase 2 began when the 7-day moving average exceeded 1 kt day^{-1} and did not drop below this threshold for more than 8 consecutive days. Manam emitted 539.9 ± 10.6 kt of SO_2 over 120 days, with a time-averaged flux of 4.72 kt day^{-1}, during Phase 2 (Fig. 5e). This period contained relatively few eruptive events with 5 minor eruptions and 1 major eruption on 28 June 2019. Despite the lower eruption frequency, SO_2 emissions prior to the major eruption were elevated substantially above the Phase 1 time-averaged flux. A total of 325.8 ± 7.6 kt SO_2 was released prior to the 28 June 2019 eruption, with most of these emissions not linked with documented eruptions. The 28 June 2019 eruption alone emitted 58.3 ± 0.5 kt of SO_2 and 82.1 ± 0.4 kt released over the following 4 days.

Phase 3: 21 July–16 October 2019

Phase 3 SO_2 emissions were reduced relative to Phase 2 with a total emitted mass of 127.9 ± 4.1 kt over 87 days and a time-averaged flux of 1.5 kt day^{-1} (Fig. 5e). However, emissions remained elevated above the background flux observed during Phase 1. Phase 3 emissions were mostly independent of eruptive activity, with only 3 minor eruptions occurring during this time.

Phase 4: 17 October 2019–31 December 2021

Phase 4 began when the 7-day moving average fell below 1 kt day^{-1} for 10 consecutive days and remained consistently below this threshold for the remainder of the time series. Phase 4 SO_2 emissions were 565.1 ± 24.9 kt over 806 days, with a time-averaged flux of 0.68 kt day^{-1} (Fig. 5e). This flux is comparable to that observed in Phase 1, and therefore, we interpret these two phases as representative of the stable background SO_2 emission rate. The small peaks in SO_2 emissions during Phase 4 are associated with the 27 minor and 2 major explosive eruptions during this period.

Thermal anomalies

Thermal emissions have been detected at Manam sporadically since MODIS coverage began in 2002. During this study period, thermal emissions are characterised by periods of frequent elevated VRP, separated by intervals of several months to years with no detectable thermal output (Fig. 5d). The time series is grouped into three discrete clusters of elevated VRP, where each cluster includes at least 5 thermal anomalies separated by intervals of no longer than 60 days.

The MODIS cloud mask shows that Manam's craters were obscured by cloud cover on 1171 days of the study period (69%) (Table S1) with thermal anomaly detections occurring on 44 cloud-covered days (3%) (Table S1). Manam's craters were cloud-free on 455 days (28%) of which thermal anomalies were detected on 31 days compared to 424 days with no detection (Table S1). Cloud cover substantially obscures direct observation of Manam's craters over the study period and therefore likely contributes to an overall under-reporting of anomaly detections. However, given that 93% of cloud-free days did not result in thermal anomaly detection, we remain confident that varying cloud cover is not modulating the temporal trends on thermal emissions that we observed. Instead, this analysis implies that the clusters identified in Fig. 5d are related to true periods of enhanced thermal emissions rather than low cloud cover and can therefore be used to infer volcanic processes.

Cluster 1: 7 August 2018–18 July 2019

Cluster 1 began 3 days prior to the onset of explosive eruptive activity in August 2018 and is linked to the eruptions during late 2018 and early 2019. Thermal anomalies became more sporadic in May 2019 but subsequently increased in frequency coinciding with a series of eruptions in June 2019 that culminated in the 28 June 2019 major eruption. Cluster 1 contains 44 detected anomalies, 18 of which are classified as high intensity and are associated with explosive eruptions (Fig. 5d). Two anomalies are classified as very high intensity and are both coincident with extensive lava flows that almost reached the coastline on 30 September 2018 (2211 MW) and between 8 and 11 January 2019 (1371 MW).

Cluster 2: 29 July–8 September 2020

Cluster 2 includes 5 low- to moderate-intensity thermal anomalies ranging between 8 and 50 MW. These detections coincide with a period of minor explosive eruptions reported between July and September 2020 (Fig. 5d).

Cluster 3: 19 June–21 December 2021

Cluster 3 occurred during a period of unrest that began in June 2021 continuing throughout the remainder of 2021. The cluster began with a series of low- to moderate-intensity thermal anomalies following a minor explosive eruption on 23 June 2021. Increased thermal emissions in August 2021 were reflected in 11 anomalies, which included three high-intensity detections. Four moderate- to high-intensity anomalies were detected following reports of Strombolian activity on 18 October 2021 and prior to the 20 October 2021 major eruption. Several low to moderate anomalies were detected in late November to December 2021 in the weeks prior to another major eruption on 22 December 2021 (Fig. 5d).

Surface temperatures

Through the period of observation, Main and South Crater were completely obscured by cloud (meteorological or volcanic) in approximately 75% of the 277 Sentinel-2/MSI images available (Fig. 5b). Surface temperatures were therefore calculated for Main and South Craters from 68 and 71 images, respectively. The daily maximum PIT for Main Crater ranged from 340 ± 83 °C to 509 ± 124 °C and 335 ± 79 °C to 510 ± 124 °C for South Crater (Fig. 5a). The mean inter-crater maximum PIT divergence was 31 °C and a maximum of 158 °C where the temperature of both craters could be measured together with South Crater having a higher maximum PIT 40 of 60 days, just 18 of these exceeding the mean inter-crater divergence. There was just one occurrence where Main Crater maximum PIT exceeded South Crater by more than the mean divergence, a 57 °C difference on 27 September 2018 during the emplacement of a lava flow from Main Crater (Fig. 5a).

The maximum South Crater PIT during the study period was measured on 20 May 2019, but the Main Crater was cloud-covered at the time, preventing direct comparison. However, the following simultaneous measurement of both craters—on 30 May 2019—has the second highest inter-crater temperature divergence of 122 °C. A bright hotspot at South Crater in MSI thermal imagery was observed on this date and follows UAS in situ observations of shallow magma within South Crater on 22 May 2019 (Liu et al. 2020). Cloud-cover prevented MSI measurements throughout June 2019, and therefore, the 28 June 2019 major eruption is not captured in this time series. However, following this eruption, a further two maximum pixel-integrated temperatures of 500 and 501 °C, with means of 455 and 473 °C, were measured at South Crater on 14 July and 19 July 2019, respectively. This suggests a period of extended high temperatures at South Crater through May to July 2019, during which a major eruption occurred. The mean PIT on 13 August 2019 (403 °C) and 18 August 2019 (408 °C) decline more substantially than the maximum temperatures, 497 °C and 475 °C respectively, compared to the two retrievals in July (Fig. 5a). As the difference between maximum and mean PIT is indicative of the spatial distribution of the hot radiating surface, we interpret this result to indicate that although hot material remained in South Crater, it likely occupied a smaller portion of the crater area.

Estimated volumes of degassed and erupted magma

The TROPOMI measured SO_2 emissions were 1432 ± 48 kt of SO_2 between 6 May 2018 and 31 December 2021 implying degassing of 0.12 to 0.22 km^3 of magma (Eq. 5) (Table 1). The magma volumes required to yield the cumulative SO_2 emissions for each degassing phase are summarised in (Table 1). It is, however, recognised that these estimates are likely to be conservative due to cloud cover inhibiting or obscuring SO_2 plumes. Over the same time period, the estimated erupted magma was 0.25 km^3 (Table 2) with explosively erupted magma contributing 95% (0.24 km^3) and effusively erupted magma 5% (0.01 km^3) of the total erupted volume. The erupted volumes contributed by each phase are given in Table 2.

Discussion

Coupling between SO_2 and thermal emissions

We present a combined time series of SO_2 and thermal emissions (Fig. 5), which are key parameters for observing changes in open-vent activity where an established connection exists between a shallow reservoir and the surface (Wright et al. 2004; Sparks et al. 2012; Pyle et al. 2013; Blackett 2013; Aiuppa 2015). Thermal anomalies associated with volcanic edifices may indicate that magma is at or near the surface (Coppola et al. 2012; Dehn and Harris, 2015; Harris 2013), and SO_2 emissions provide an insight

Table 1 Summary of SO_2 emissions by phase and the calculated magma volume required to supply observed SO_2 emissions

Phase	Duration (days)	Total SO_2 emitted (kt)	Mean daily SO_2 flux (kt day^{-1})	Total magma volume (km^3)	Mean magma volume (km^3 day^{-1})
1	319	199 ± 8	0.62 ± 0.03	1.7 – 3.0 × 10^{-2}	0.5 – 1.7 × 10^{-4}
2	120	540 ± 11	4.72 ± 0.09	4.6 – 8.1 × 10^{-2}	3.8 – 12.1 × 10^{-4}
3	87	128 ± 4	1.5 ± 0.05	1.1 – 1.9 × 10^{-2}	1.3 – 3.9 × 10^{-4}
4	806	565 ± 25	0.68 ± 0.03	4.9 – 8.5 × 10^{-2}	0.6 – 1.9 × 10^{-4}
All	1332	1432 ± 48	1.1 ± 0.04	1.2 –2.2 × 10^{-1}	0.9 – 2.9 × 10^{-4}

Table 2 Volume of erupted magma by phase. Explosive erupted volumes calculated from eruption column heights using Eq. 6 (Mastin et al. 2009). Eruption column heights recorded by Darwin VAAC and the Rabaul Volcanological Observatory observer on Manam. Effusive eruptions are estimated from satellite observation of lava flows and a representative thickness calculated from an orthomosaic from the September to October 2018 lava flow against an older digital elevation model (see supplementary material) and using a measured porosity (18.8%) from the September to October 2018 lava flow

	Erupted volume (km^3)			
Phase	Explosive	Effusive	Total	Percentage
1	1.7×10^{-1}	6.5×10^{-3}	1.8×10^{-1}	70%
2	3.1×10^{-2}	4.6×10^{-3}	3.6×10^{-2}	14%
3	1.9×10^{-3}	4.8×10^{-4}	2.4×10^{-3}	1%
4	3.7×10^{-2}	7.8×10^{-4}	3.8×10^{-2}	15%
All	2.4×10^{-1}	1.2×10^{-2}	2.5×10^{-1}	

into conduit permeability (Edmonds et al. 2003), magma convection (Shinohara 2008), and the volume of degassing magma present at shallow depths (Allard et al. 1994; Aiuppa et al. 2017).

Thermal and SO_2 emissions have been shown to be coupled during a background-level activity at open-vent systems such as Stromboli (Italy) (Laiolo et al. 2022, 2018), Bagana (Papua New Guinea) (McCormick et al. 2012; McCormick Kilbride et al. 2019), Batu Tara (Indonesia) (Laiolo et al. 2018), Tinakula (Solomon Islands) (Laiolo et al. 2018), and Mt. Etna (Italy) (Coppola et al. 2019; D'Aleo et al. 2019). Contrastingly, periods of uncoupled behaviour between these two parameters can signal transient disturbances to the magmatic system. At Stromboli, elevated SO_2 emissions generally lag behind peaks in thermal emissions associated with paroxysms and lava flows (Laiolo et al. 2022). Periods of high SO_2 flux but low radiant heat flux during quiescence phases are typically attributed to unerupted magmatic intrusions (e.g., Mt. Etna 2005–06, Coppola et al. 2019). Conversely, periods of below-average SO_2 flux but high radiant flux have been explained by the extrusion of previously degassed magma (e.g., Tinakula 2006–2012, Laiolo et al. 2018).

Here, we evaluate the degree to which the SO_2 and thermal emission time series at Manam are coupled for each of the four degassing phases (Fig. 5). The correlation between thermal and SO_2 emissions is calculated using moving weekly total emissions as it allows the mostly continuous SO_2 flux to be compared to the intermittent thermal emissions. The correlation between total weekly SO_2 emissions and total weekly VRP is weak for the entire time series with a correlation coefficient (r) of 0.12 (Fig. S3). Emissions have a moderately weak correlation ($r = 0.34$) in Phase 1, with Phase 2 emissions having a moderately strong positive correlation ($r = 0.74$) (Fig. S3). Phases 3 and 4 emissions are very weakly correlated ($r = 0.07$). The weak correlations in Phase 1 are likely due to the fact that peak VRPs are associated with lava effusions, whereas peak SO_2 emissions typically coincide with explosive eruptions, as well as the fact that SO_2 emissions vary over 3 orders of magnitude (0.92–58 kt) compared to 4 for thermal emissions (5–2792 MW). However, the strong positive correlation in Phase 2 reflects the periods of sustained elevated SO_2 emissions alongside regular thermal anomalies with peaks in total emissions around the 28 June 2019 eruption.

While the correlation between the magnitude of the two parameters is weak for most of the time series, the temporal relationship between SO_2 and thermal emissions throughout the time series can be used to interpret processes governing the observed activity. We note that a limitation for comparing these emissions is that the overpasses for MODIS and TROPOMI are at different times of day and so represent different snapshots in time of the emissions. However, given the assumed 1-day atmospheric residence time of SO_2, it remains reasonable to compare the SO_2 and thermal emissions as a true reflection of Manam's open-vent activity within a 24-h period.

Throughout Phase 1, peaks in SO_2 emission occurred coincident with periods of heightened radiant flux and were typically aligned with an observed eruption (Fig. 5). On five occasions, thermal anomalies began to be detected days to weeks ahead of eruptions with coincident elevated SO_2 emissions (e.g., August 2018, October 2018, December 2018, January 2019, and March 2019; Figs. 5 and S2). This was not the case for the 8 January and 23 January 2019 eruptions, where SO_2 emissions peaked without thermal anomaly detections, likely due to the presence of cloud and the ash-rich plume obscuring thermal detections.

The elevated outgassing characterising Phase 2 (4.72 ± 0.09 kt day^{-1}) occurred alongside four thermal anomalies in March–May 2019, one of which was coincident with an above-average SO_2 emission. Magma was observed in situ deep within South Crater on 22 May 2019 (Liu et al. 2020), but no anomaly was detected (Fig. 5e), likely due to cloud cover obscuring the summit at the time of the satellite overpass (10:30 AM and 1:30 PM). MSI SWIR hotspots were observed on 20 May and 30 May 2019, both with high surface temperatures (Fig. 5a), which suggest similar conditions were likely present on 22 May 2019. MODIS acquisitions were affected by cloud cover with the summit being obscured 21 of 30 days in June, suggesting a possible under-reporting in the frequency of thermal anomaly detections during this period. The frequency of thermal anomalies increased in June 2019 alongside an increase in eruptive activity compared to the prior 2 months, including the 28 June 2019 major eruption. Following an 11-day period of subdued SO_2 emissions between 3 and 13 June 2019, during which <7 kt was emitted over 9 days, elevated gas emissions are resumed alongside the escalating frequency of thermal anomalies. Given the temporal correlation of emissions alongside the strong weekly moving total emission correlation, it is suggested that Phase 2 represents another period of coupled emissions.

Elevated SO_2 emissions continued in Phase 3 (1.5 ± 0.05 kt day^{-1}) but were much reduced compared to Phase 2. Only one thermal anomaly was detected coinciding with an SO_2 emission of 1.9 kt on the day of a minor eruption on 29 September 2019 (Fig. 5). Overall, Phase 3 represents an extended period where gas and thermal emissions appear to be decoupled, though both parameters appear to be declining in intensity.

SO_2 emissions in Phase 4 ($\sim 0.68 \pm 0.03$ kt day^{-1}) returned to a comparable level to Phase 1 ($\sim 0.62 \pm 0.03$ kt day^{-1}). Phase 1 exhibited a correlation both temporally and in magnitude between thermal and SO_2 emissions, but this is not the case in Phase 4. Although instances where thermal anomalies coincide with above-average SO_2 emissions occur (e.g., 20 October 2021), most above-background emissions occur when no thermal anomalies are detected. During thermal clusters 2 and 3, the magnitude of SO_2 emissions remains unchanged relative to outside these periods of heightened thermal emissions (Fig. 5).

Consequently, we propose that both coupled and decoupled regimes in SO_2 and thermal emissions are present within the study period and that a transition from coupled to decoupled behaviour occurred following the 21 July 2019 eruption at the beginning of Phase 3. Phases 1 and 2 operate under the coupled regime, where peaks in the two parameters are well correlated. In contrast, Phases 3 and 4 show little to no correlation between either the timing or magnitude of thermal and gas emissions and therefore represent a decoupled regime.

Is persistent outgassing balanced by magma flux?

Mass balance calculations at mafic open-vent volcanoes, globally, suggest that the amount of magma required to sustain observed gas fluxes is generally far greater than that erupted (Edmonds et al. 2022b; Kazahaya et al. 1994; Laiolo et al. 2022; McCormick et al. 2012). Constraining the mass balance of magma in terms of total inputs and outputs, and variations over time, is key to relating observed gas emissions to the magmatic and eruptive processes operating at open-vent volcanoes. SO_2 emissions and radiant flux can be used to infer the amounts of magma supplied to the shallow magmatic system (input) and erupted (output), respectively (Harris et al. 1999; Coppola et al. 2019).

Over the duration of the study period, the estimated erupted magma (output) was ~ 0.25 km^3, and the estimated degassed magma (input) was 0.12–0.22 km^3. The estimated magma input and maximum output are very similar, suggesting no significant excess or deficit in the magma flux balance over the entire time series, especially given the associated uncertainties with the pre-eruptive S content, impact of clouds on TROPOMI SO_2 retrievals, and the relationship between eruption column high and erupted mass. However, the magma input value is likely to fall somewhere between the minimum and maximum estimate, indicating that a deficit in magma supply is more likely than a state of excess degassing over the entire study period.

Examining the magma balance for each degassing phase reveals that the eruptions during Phase 1 were responsible for 70% of the erupted magma over the entire time series (Fig. 6a). In contrast, the supply of magma was relatively steady, as indicated by the consistent cumulative magma input gradient in Phases 1, 3, and 4 (Fig. 6a). The daily magma net balance shows a steady low magma supply indicated by Manam's persistent degassing alongside intermittent high magnitude magma outputs (Fig. 6b).

Interpretation – a magma recharge event captured from space?

Here, we interpret the observed SO_2 and thermal emissions, the coupling of these parameters, and the estimated magma flux balance within the context of a magma recharge event to examine the processes and feedback at work throughout the study period.

In this section, we infer periods of high pressure from thermal anomaly detections and their possible relation to the varying height of the magma column. The height of magma columns and lava lakes can vary substantially over days to months, and this is particularly well observed in open-vent systems. At open-vent systems like Manam, where the magmatic system is open to the atmosphere, variations in magma column height have been interpreted to reflect changing pressure within the shallow magma reservoirs (Patrick et al. 2015; Moussallam et al. 2016; Lev et al. 2019, Calvari et al. 2011, Johnson et al. 2018). High system pressure is reflected in an elevated magma column, which may rise high enough to be detected as a thermal anomaly and, in some cases, visible within the crater. Conversely, lower pressure in the magmatic system results in the magma column being too deep to be detected as a thermal anomaly. While eruptions are associated with high-pressure conditions, lava effusions typically produce high VRP due to their large radiating surface (Blackett 2017), and anomalies linked to explosive eruptions have high VRP due to the radiated heat of large volumes of magma being ejected. Therefore, only non-eruption-related thermal anomalies are used here to indicate relative pressure.

The 10 August 2018 eruption ended 11 months of quiescence and passing degassing following the end of the 2017 eruptive period on 10 September 2017 (Global Volcanism Program 2021a). The absence of thermal anomalies during

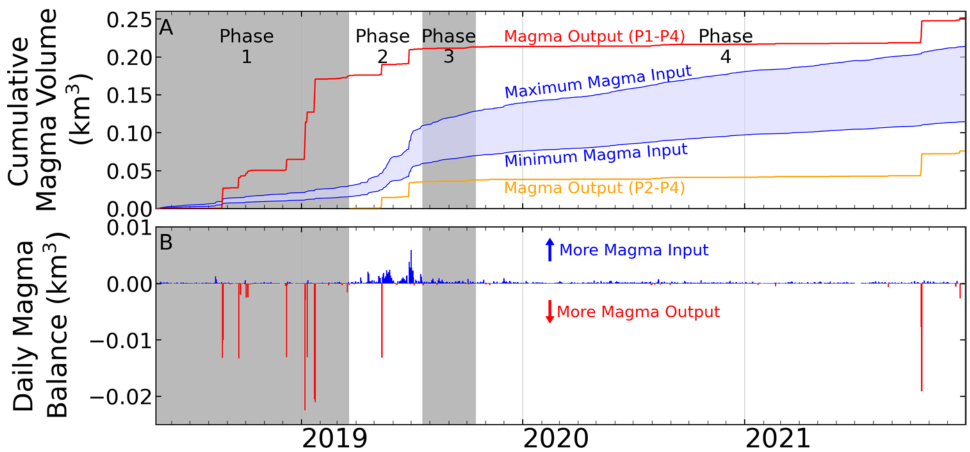

Fig. 6 **A** Cumulative magma output (i.e., effusively and explosively erupted magma) (red) and cumulative magma input (magma reaching the exsolution level for SO_2 at depth) (blue). The minimum and maximum magma input values are based on varying the assumed sulphur content (0.2 ± 0.02 wt%) and vesicularity (0–30%) of the melt used in the petrological method to calculate magma volumes from SO_2 flux (Devine et al. 1984). **B** The daily net magma balance is calculated as magma output volume subtracted from magma input volume

this inter-eruptive period (Fig. 5e) suggests a low magma column level and therefore low system pressure. We infer that residual magma from the 2017 eruptive period continued to degas over this period, sustaining the observed SO_2 emissions and driving sluggish convection in the shallow plumbing system (Kazahaya et al. 1994; Allard 1997; Witter et al. 2004; Beckett et al. 2014). However, continued degassing of this residual magma without replenishment would drive volatile depletion, cooling, and crystallisation, initially limiting the mobility of melts and subsequently the permeable migration of exsolved fluids (Edmonds et al. 2022b). Formation of a crystal-rich, semi-permeable cap may be partially responsible for the absence of thermal anomalies in the interruptive period (Stix et al. 1997; Diller et al. 2006; Hall et al. 2015; Gaunt et al. 2020).

In this context, we interpret that the time-averaged Phase 1 SO_2 emissions of ~ 0.62 kt day^{-1} represent the supply of volatiles derived from the second boiling of residual magma, migrating slowly through the semi-permeable cap (Fig. 7a). Thermal anomalies were first detected on 7 August 2018 (Fig. 5d), indicating increasing pressure which was followed by the series of explosive and effusive eruptions in August–September 2018. This increased pressure was likely caused by a volatile-rich magma recharge (Andronico and Corsaro, 2011; Grapenthin et al. 2022; Patrick et al. 2019a, 2015; Viccaro et al. 2015) that would have begun arriving at the shallow storage region several months prior to the onset of eruptive activity based on estimates from similar systems (Cannata et al. 2018; Aiuppa et al. 2021; Petrone et al. 2022). The presence of the semi-permeable cap would have initially inhibited pressure release (Diller et al. 2006; Battaglia et al. 2019), but continued increasing pressure would eventually exceed the cap's strength (Woitischek et al. 2020), causing fracturing and complete failure, resulting in the 10 August 2018 eruption. The 13 August 2018 lava effusion (Global Volcanism Program 2021a) via the reopened conduit would have further decreased pressure in the magmatic system.

During Phase 1, we calculate that 0.18 km^3 of magma was erupted, compared to 0.03 km^3 required to sustain the observed gas emissions (Fig. 6, Table 2); this result implies that the erupted magma was extensively degassed prior to eruption. We interpret that the degassed residual magma continued to be removed by the August and September 2018 eruptions (Fig. 7b), including the 25 August 2018 major explosive eruption and the intermittent effusive activity from 9 September to 1 October 2018 (Fig. 5). The eruptive activity in January 2019 removed an estimated 0.11 km^3 (42% of the estimated total erupted material during this study) and therefore likely expelled most of the remaining residual magma. The elevated SO_2 emissions of Phase 2 commenced following the 29 March 2019 eruption that removed the final remnants of 2017 residual magma and re-established an open conduit state. Removing residual magma present within the conduit would have reduced the lithostatic load in the upper magmatic system, thereby promoting continued ascent of volatile-rich recharge magma (Calvari et al. 2011) and a positive feedback between magma ascent, decompression, and volatile exsolution.

During Phase 2 (March–July 2019), we estimate that 0.08 km^3 of magma entered the shallow plumbing system compared to 0.04 km^3 erupted, indicating Manam was in a state of open-vent excess degassing (Rose et al. 2013; Edmonds et al. 2022b; Vergniolle and Métrich 2022). In situ observations of magma within South Crater on 22 May 2019 and two high surface temperature retrievals on 20 and 30 May 2019

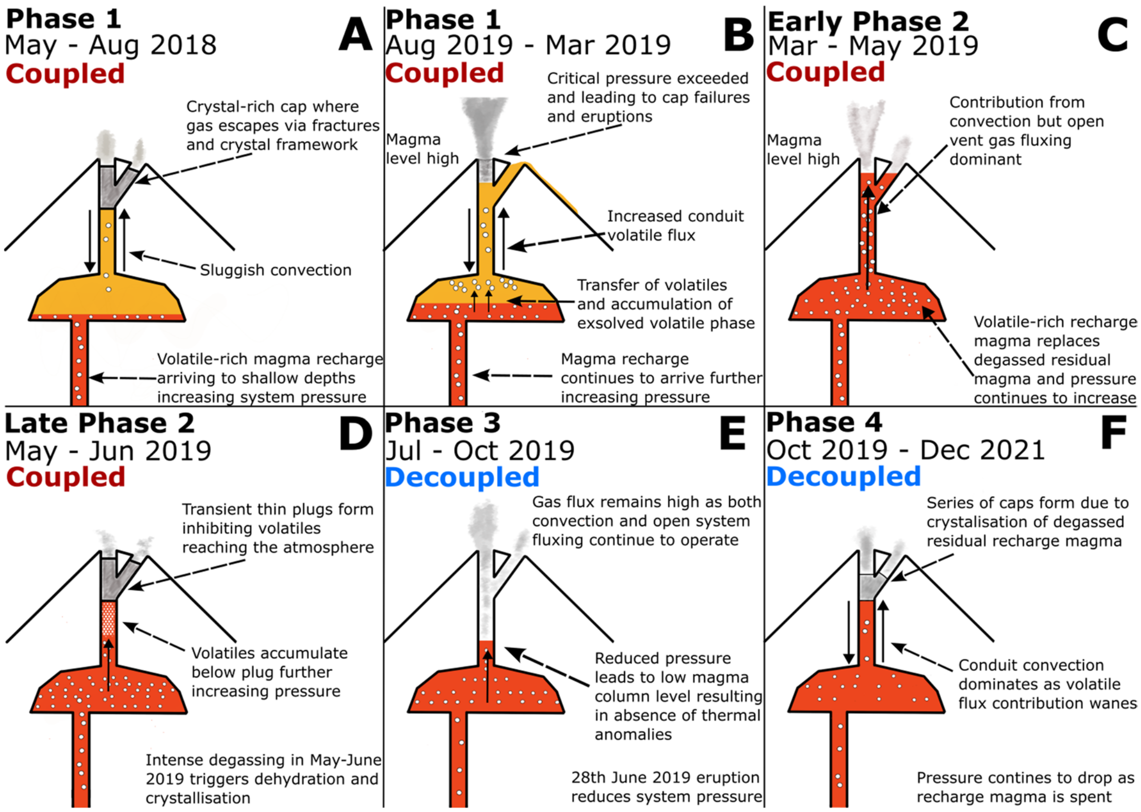

Fig. 7 Conceptual model of Manam's shallow plumbing system and processes responsible for the observed activity, thermal anomalies, and SO_2 emissions. "Coupled" and "Decoupled" indicate the relationship between thermal and SO_2 emissions during each phase; see main text for detail

(Fig. 5a) suggest at least transient periods of high pressure raising the magma column. Unlike Phase 1, increased SO_2 emissions are not explicitly linked to eruptions or to thermal anomaly detections; therefore, we suggest that surface outgassing involved an enhanced contribution from open system fluxing of volatiles independent of magma ascent, transferred from degassing of recharge magma within the shallow reservoir (Edmonds et al. 2022b).

The latter stage of Phase 2 (June–July 2019) (Fig. 7d) displayed increased thermal emissions and eruptive activity compared to earlier in Phase 2. Two surface temperature measurements of > 450 °C in South Crater (Fig. 5a) alongside increased frequency of thermal anomaly detections and recorded eruptions suggest that the magma level remained high in the conduit caused by high reservoir pressure. A marked reduction in daily SO_2 emissions, albeit alongside above-average mean cloud fraction (0.6–0.7) (Fig. S1), around early June suggests that permeability within the conduit briefly decreased (Fig. 5). However, the subsequent return to elevated outgassing levels following the 7 June 2019 eruption suggests that explosive activity may have reopened degassing pathways. We propose that the intense degassing and resulting dehydration-driven crystallisation during Phase 2 may have promoted the development of another cap (Applegarth et al. 2013; Couch et al. 2003; Gaunt et al. 2020; Lipman et al. 1985), reducing the permeability of the magma and consequently promoting gas accumulation beneath the cap (Stix et al. 1997; Sparks 1997; Burgisser et al. 2011). Three minor explosive eruptions on 7, 8, and 18 June 2019 are likely evidence of increasing strain on the cap, but it appears that each failed to fully re-open the conduit. We attribute the 28 June 2019 major eruption to the eventual catastrophic failure of this cap, releasing accumulated volatiles and triggering rapid downward-propagating decompression. Explosive activity during this event generated a 15.2 km eruption column, released 58.3 kt of SO_2, and erupted ~ 0.018 km^3 of magma (7% of the estimated total erupted material during this study period).

SO_2 emissions during Phase 3 remained above background levels but reduced from ~ 4.72 kt day^{-1} to ~ 1.54 kt day^{-1}, which may reflect a gradual depletion of volatiles in the shallow magmatic system. SO_2 and thermal emissions remained decoupled in Phase 3. To explain the low frequency of both thermal anomalies and reported eruptions, we infer that the removal of a substantial volume of magma and volatiles would have reduced the pressure in the shallow magmatic system considerably (Anderson et al. 2015; Patrick et al. 2020; Barrière et al. 2022) (Fig. 7e). The fact that surface SO_2 emissions were sustained at elevated fluxes throughout this period (Fig. 5e) signals that conduit convection and volatile fluxing remained active despite the reduction in system pressure. During this period, SO_2 emissions imply that 0.02 km^3 of magma was supplied compared to just 0.002 km^3 being erupted (Table 2), indicating that Manam maintained a state of open-vent excess degassing.

Average daily SO_2 emissions in Phase 4 (~0.68 kt day^{-1}) returned to similar levels to Phase 1 (~0.62 kt day^{-1}), which can be considered a return to background degassing levels. Reservoir pressure was likely low during November 2019 to May 2021 since there were just 5 thermal anomaly detections (Cluster 2) associated with a series of 6 minor eruptions in July–September 2020. The return to background SO_2 emissions suggests that the initially volatile-rich recharge magma had become relatively depleted. The dominant process responsible for volatile transport would likely have reverted from volatile fluxing to conduit convection, where gas emissions were once again tied to magma transport within the conduit (Fig. 7f) (Beckett et al. 2014; Edmonds et al. 2022b). This is supported not only by the decrease in SO_2 emissions compared to the previous two phases (Fig. 3) but also by the reduction in excess degassing with 0.09 km^3 of magma supplied compared to 0.04 km^3 erupted, approximately 75% of which was erupted between August and December 2021.

Together, the sparsity of thermal anomalies prior to the onset of Cluster 3 in August 2021 alongside the persistent background SO_2 emissions indicates that emissions were decoupled during Phase 4 (Fig. 5). The Cluster 3 thermal emissions suggest that Manam was periodically experiencing high pressure throughout the second half of 2021, raising the magma column level close to the surface. These anomalies were associated temporally with the eruptive activity reported throughout this period, yet most were not linked to substantial SO_2 emission peaks as had been the case during Phase 1 (Fig. 5). As such, we interpret that the transient periods of eruptive activity during this background level degassing phase are unlikely to reflect a further recharge of volatile-rich magma reaching the shallow plumbing system. Instead, the lack of SO_2 emissions indicates the involvement of comparatively volatile-depleted magma, where the increased pressure to drive explosive events is more likely the result of reduced conduit permeability through cooling and dehydration-driven crystallisation of the residual unerupted magma (Applegarth et al. 2013; Lipman et al. 1985). A repeating cycle of partial closing and re-opening of the conduit continued throughout the remainder of 2021, with more substantial and protracted reductions in permeability likely preceding the major eruptions on 20 October and 22 December 2021 (Hall et al. 2015; Battaglia et al. 2019).

Long-term SO_2 emission variability

The time series of SO_2 emissions at Manam presented here (Fig. 5e) demonstrates the variability of volcanic volatile emissions over months to years, even at persistently degassing volcanoes. The annual mean daily SO_2 emissions (based on a 1-day residence time) are presented alongside the annual mean daily SO_2 emissions (2005–2015) first reported by Carn et al. (2017) in Fig. 8. Carn et al. (2017) identified a declining trend in annual SO_2 emissions, and the inclusion of the data from this study shows that this declining trend continues despite the elevated emissions during 2019 (Fig. 8). The 2019 annual daily mean emissions of 2.2 kt day^{-1} substantially exceed the 2015–2021 mean (1.4 kt day^{-1}) and represent a striking departure from the long-term trend to which emissions in 2020 and 2021 return (Fig. 8). This observation demonstrates how open-vent volcanoes, such as Manam, can exhibit wide fluctuations in emissions, which are superimposed on decadal trends. If placed within the global SO_2 inventory compiled by Carn et al. (2017), Manam's SO_2 emissions would be ranked 31st in Phase 1, 3rd in Phase 3, 10th in Phase 3, and 25th in Phase 4 (Table S4). This variability has also been recognised at other

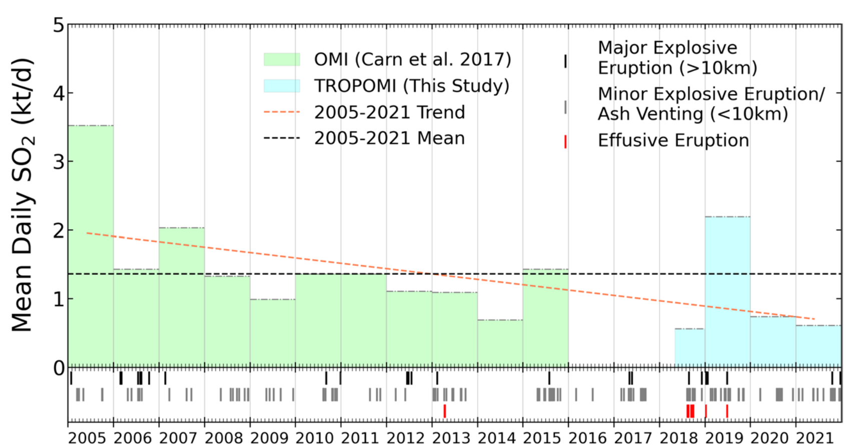

Fig. 8 Manam annual daily SO_2 emissions (kt/d) measured using OMI (Ozone Monitoring Instrument) (green) (Carn et al. 2017), TROPOMI derived annual daily SO_2 emissions based on a 1-day residence time (blue) (this study), mean daily SO_2 trend calculated by fitting a first order polynomial to the time series (orange dotted line), and mean annual emissions 2015 to 2012—1.36 kt/d (black dotted line)

open-vent systems, including Bagana (Papua New Guinea; McCormick Kilbride et al. 2023), and consequently highlights the inherent limitations and uncertainties associated with compiling global volcanic volatile inventories, especially where short duration or campaign measurements are relied upon. Additionally, this analysis emphasises the need for a multi-parametric approach to interpreting changes in degassing behaviour and eruptive activity at open-vent volcanic systems, as the processes responsible for modulating degassing are varied and interpretations potentially ambiguous when derived from emission rates alone.

Conclusions

We have used a multi-parameter remote sensing approach to investigate the subsurface processes responsible for the period of elevated volcanic activity observed at Manam between August 2018 and December 2021. Using satellite-based measurements of thermal and sulphur dioxide (SO_2) emissions, combined with in situ observations of volcanic activity, we quantify the relative inputs and outputs of magma and gas to the shallow conduit and surface—and consequently the varying extent of excess degassing through time.

From these time series, four distinct phases of volcanic activity are identified between 2018 and 2021. To explain these phases in the context of volcanological processes, we propose that eruptive activity at Manam during the period of observation was driven by the injection and eruption of a volatile-rich recharge magma. In this conceptual model, initial eruptions in August 2018—triggered by positive reservoir pressure changes after a year-long period of repose—removed previously degassed residual magma to re-open the conduit and promote efficient fluxing of segregated volatiles through the shallow magmatic system, accounting for the very high SO_2 fluxes (4.72 kt day^{-1}) observed in March–June 2019. A period of lower emissions, both thermal and SO_2, immediately prior to the major eruption on 28 June 2019 points to reduced permeability and ultimately failure of a conduit cap as a likely trigger mechanism. We suggest cap formation may have been promoted by the extended period of enhanced degassing and resulting dehydration-driven crystallisation in the shallow conduit.

The multi-parameter time series has allowed the estimation of Manam's magma budget and resolved the previously unknown fate of the magma supplying Manam's high SO_2 flux in 2019 (Liu et al. 2020). Overall, we calculate that the magma output exceeds the magma input if we consider the entire time series examined in this study. However, since this output component is dominated by eruptions from August 2018 to March 2019—which we infer to involve residual degassed magma from 2017—this suggests that the magma budget is balanced over long timescales and that degassed magma is eventually erupted at Manam rather than intruded.

In the context of long-term SO_2 degassing trends, the period of enhanced degassing in 2019 is superimposed on a long-term declining trend in emissions at Manam and is therefore not representative of the time-averaged degassing behaviour of this volcano. This substantial temporal variability is not unique to Manam and has been recognised at other strong open-vent emitters (e.g., Bagana, Papua New Guinea, McCormick Kilbride et al. 2023). These observations highlight an important limitation to acknowledge when extrapolating short-term or campaign measurements at open-vent volcanoes to long-term emissions contributions within global volcanic volatile inventories.

Supplementary Information The online version contains supplementary material available at https://doi.org/10.1007/s00445-024-01772-2.

Acknowledgements The authors wish to thank Ima Itikarai and Kila Mulina (Rabaul Volcanological Observatory) for providing a sample of the 28 June 2019 lava flow. We acknowledge Keiran Wood (University of Manchester) who piloted the Unoccupied Aerial System, which captured footage of Manam, which was used to create the orthomosiac model of the October 2018 lava flow.

Author contribution AC, EN, and CK contributed to this study conception and design. Material preparation, data collection, and analysis were performed by AC and EN. Sentinel-5P TROPOMI SO_2 mass retrieval process was provided by CH. The first draft of the manuscript was written by AC, and all authors commented on the previous versions of the manuscript. All authors read and approved the final manuscript.

Funding This work was supported by the UK Natural Environment Research Council (grant no. NE/S007229/1).

Declarations

Conflict of interest The authors declare no competing interests.

References

Abbott LD, Silver EA, Galewsky J (1994) Structural evolution of a modern arc-continent collision in papua NewGuinea. Tectonics 13(5):1007–34. https://doi.org/10.1029/94TC01623

Abbott LD (1995) Neogene tectonic reconstruction of the Adelbert-Finisterre-New Britain Collision, Northern Papua New Guinea." Journal of Southeast Asian Earth Sciences 11(1):33–51.https://doi.org/10.1016/0743-9547(94)00032-A

Aiuppa A (2015) Volcanic-gas monitoring. In: Volcanism and Global Environmental Change. Cambridge University Press, pp 81–96

Aiuppa A, Bitetto M, Francofonte V et al (2017) A CO2-gas precursor to the March 2015 Villarrica volcano eruption. Geochem Geophys Geosystems 18:2120–2132. https://doi.org/10.1002/2017GC006892

Aiuppa A, Fischer TP, Plank T, Bani P (2019) CO2 flux emissions from the Earth's most actively degassing volcanoes, 2005–2015. Sci Rep 9:5442. https://doi.org/10.1038/s41598-019-41901-y

Aiuppa A, Bitetto M, Delle Donne D et al (2021) Volcanic CO2 tracks the incubation period of basaltic paroxysms. Sci Adv 7:eabh0191. https://doi.org/10.1126/sciadv.abh0191

Allard P (1997) Endogenous magma degassing and storage at Mount Etna. Geophys Res Lett 24:2219–2222. https://doi.org/10.1029/97GL02101

Allard P, Carbonnelle J, Métrich N et al (1994) Sulphur output and magma degassing budget of Stromboli volcano. Nature 368:326–330. https://doi.org/10.1038/368326a0

Allard P, Burton M, Muré F (2005) Spectroscopic evidence for a lava fountain driven by previously accumulated magmatic gas. Nature 433:407–410. https://doi.org/10.1038/nature03246

Anderson KR, Poland MP, Johnson JH, Miklius A (2015) Episodic deflation–inflation events at Kīlauea volcano and implications for the shallow magma system. In: Hawaiian Volcanoes. American Geophysical Union (AGU), pp 229–250

Andres RJ, Kasgnoc AD (1998) A time-averaged inventory of subaerial volcanic sulfur emissions. J Geophys Res Atmospheres 103:25251–25261. https://doi.org/10.1029/98JD02091

Applegarth LJ, Tuffen H, James MR et al (2013) Direct observations of degassing-induced crystallization in basalts. Geology 41:243–246. https://doi.org/10.1130/G33641.1

Applegarth LJ, Tuffen H, James MR, Pinkerton H (2013) Degassing-Driven Crystallisation in Basalts. Earth-Sci Rev 116:1–16. https://doi.org/10.1016/j.earscirev.2012.10.007

Barrière J, d'Oreye N, Smets B et al (2022) Intra-crater eruption dynamics at Nyiragongo (D.R. Congo), 2002–2021. J Geophys Res Solid Earth 127:e2021JB023858. https://doi.org/10.1029/2021JB023858

Battaglia J, Hidalgo S, Bernard B et al (2019) Autopsy of an eruptive phase of Tungurahua volcano (Ecuador) through coupling of seismo-acoustic and SO2 recordings with ash characteristics. Earth Planet Sci Lett 511:223–232. https://doi.org/10.1016/j.epsl.2019.01.042

Beckett FM, Burton M, Mader HM et al (2014) Conduit convection driving persistent degassing at basaltic volcanoes. J Volcanol Geotherm Res 283:19–35. https://doi.org/10.1016/j.jvolgeores.2014.06.006

Beirle S, Hörmann C, Penning de Vries M et al (2014) Estimating the volcanic emission rate and atmospheric lifetime of SO_2 from space: a case study for Kīlauea volcano, Hawai`i. Atmospheric Chem Phys 14:8309–8322. https://doi.org/10.5194/acp-14-8309-2014

Berk A, Conforti P, Kennett R, et al (2014) MODTRAN® 6: a major upgrade of the MODTRAN® radiative transfer code. In: 2014 6th Workshop on Hyperspectral Image and Signal Processing: Evolution in Remote Sensing (WHISPERS). pp 1–4

Blackett M (2013) Review of the utility of infrared remote sensing for detecting and monitoring volcanic activity with the case study of shortwave infrared data for Lascar Volcano from 2001–2005. Geol Soc Lond Spec Publ 380:107–135. https://doi.org/10.1144/SP380.10

Blackett M (2017) An overview of infrared remote sensing of volcanic activity. J Imaging 3:13. https://doi.org/10.3390/jimaging3020013

Bottinga Y, Weill DF (1970) Densities of liquid silicate systems calculated from partial molar volumes of oxide components. Am J Sci 269:169–182

Burgisser A, Arbaret L, Druitt TH, Giachetti T (2011) Pre-explosive conduit conditions of the 1997 Vulcanian explosions at Soufrière Hills Volcano, Montserrat: II. Overpressure and depth distributions. J Volcanol Geotherm Res 199:193–205. https://doi.org/10.1016/j.jvolgeores.2010.11.014

Calder ES, Cole PD, Dade WB et al (1999) Mobility of pyroclastic flows and surges at the Soufriere Hills Volcano, Montserrat. Geophys Res Lett 26:537–540. https://doi.org/10.1029/1999GL900051

Calvari S, Spampinato L, Bonaccorso A et al (2011) Lava effusion — a slow fuse for paroxysms at Stromboli volcano? Earth Planet Sci Lett 301:317–323. https://doi.org/10.1016/j.epsl.2010.11.015

Cannata A, Di Grazia G, Giuffrida M et al (2018) Space-time evolution of magma storage and transfer at Mt. Etna volcano (Italy): the 2015–2016 reawakening of voragine crater. Geochem Geophys Geosystems 19:471–495. https://doi.org/10.1002/2017GC007296

Caricchi L, Sheldrake TE, Blundy J (2018) Modulation of magmatic processes by CO2 flushing. Earth Planet Sci Lett 491:160–171. https://doi.org/10.1016/j.epsl.2018.03.042

Carn SA, Fioletov VE, McLinden CA et al (2017) A decade of global volcanic SO2 emissions measured from space. Sci Rep 7:44095. https://doi.org/10.1038/srep44095

Connell J, Lutkehaus N (2016) Another Manam? The forced migration of the population of Manam Island, Papua New Guinea, due to volcanic eruptions 2004–2005. International Organisation for Migration

Coppola D, Laiolo M, Piscopo D, Cigolini C (2013) Rheological control on the radiant density of active lava flows and domes. J Volcanol Geotherm Res 249:39–48. https://doi.org/10.1016/j.jvolgeores.2012.09.005

Coppola D, Laiolo M, Cigolini C et al (2016) Enhanced volcanic hot-spot detection using MODIS IR data: results from the MIROVA system. Geol Soc Lond Spec Publ 426:181–205. https://doi.org/10.1144/SP426.5

Coppola D, Laiolo M, Massimetti F, Cigolini C (2019) Monitoring endogenous growth of open-vent volcanoes by balancing thermal and SO2 emissions data derived from space. Sci Rep 9:9394. https://doi.org/10.1038/s41598-019-45753-4

Coppola D, Piscopo D, Laiolo M, Cigolini C, Delle Donne D, Ripepe M (2012) Radiative heat power at sStrombolivolcano during 2000–2011: twelve years of MODIS observations. J Volcanol Geotherm Res 215–216 (February 15, 2012): 48–60. https://doi.org/10.1016/j.jvolgeores.2011.12.001

Coppola D, Valade S, Masias P et al (2022) Shallow magma convection evidenced by excess degassing and thermal radiation during the dome-forming Sabancaya eruption (2012–2020). Bull Volcanol 84:16. https://doi.org/10.1007/s00445-022-01523-1

Coppola D (2022) MIROVA

Couch S, Sparks RSJ, Carroll MR (2003) The kinetics of degassing-induced crystallization at Soufrière Hills Volcano, Montserrat. J Petrol 44:1477–1502. https://doi.org/10.1093/petrology/44.8.1477

D'Aleo R, Bitetto M, Delle Donne D, Coltelli M, Coppola D, McCormick Kilbride B, Pecora E et al (2019) Understanding the SO2 degassing budget of Mt Etna's paroxysms: first clues from the December 2015 Sequence." Frontiers in Earth Science 6 https://www.frontiersin.org/article/10.3389/feart.2018.00239

Dehn J, Harris AJ (2015) Thermal anomalies at volcanoes. In: Kenneson Gene Dean Jonathan Dehn (eds) Monitoring volcanoes in the north pacific: observations from space, pp 49–78. Berlin, Heidelberg, Springer, https://doi.org/10.1007/978-3-540-68750-4_3

Devine JD, Sigurdsson H, Davis AN, Self S (1984) Estimates of sulfur and chlorine yield to the atmosphere from volcanic eruptions and potential climatic effects. J Geophys Res Solid Earth 89:6309–6325. https://doi.org/10.1029/JB089iB07p06309

Diller K, Clarke AB, Voight B, Neri A (2006) Mechanisms of conduit plug formation: implications for Vulcanian explosions. Geophys Res Lett 33:. https://doi.org/10.1029/2006GL027391

Edmonds M, Mason E, Hogg O (2022a) Volcanic outgassing of volatile trace metals. Annu Rev Earth PlanetSci 50:79–98. https://doi.org/10.1146/annurev-earth-070921-062047

Edmonds M, Liu EJ, Cashman KV (2022b) Open-vent volcanoes fuelled by depth-integrated magmadegassing. Bull Volcanol 84:28. https://doi.org/10.1007/s00445-021-01522-8

Edmonds M, Oppenheimer C, Pyle DM et al (2003) SO2 emissions from Soufrière Hills Volcano and their relationship to conduit permeability, hydrothermal interaction and degassing regime. J Volcanol Geotherm Res 124:23–43. https://doi.org/10.1016/S0377-0273(03)00041-6

Fioletov VE, McLinden CA, Krotkov N, Li C (2015) Lifetimes and emissions of SO2 from point sources estimated from OMI. Geophys Res Lett 42:1969–1976. https://doi.org/10.1002/2015GL063148

Flower VJB, Carn SA (2015) Characterising volcanic cycles at Soufriere Hills Volcano, Montserrat: time series analysis of multi-parameter satellite data. J Volcanol Geotherm Res 304:82–93. https://doi.org/10.1016/j.jvolgeores.2015.07.035

Francis PW, Rothery DA (1987) Using the Landsat Thematic Mapper to detect and monitor active volcanoes: an example from Lascar volcano, northern Chile. Geology 15:614–617. https://doi.org/10.1130/0091-7613(1987)15%3c614:UTLTMT%3e2.0.CO;2

Gaunt HE, Burgisser A, Mothes PA et al (2020) Triggering of the powerful 14 July 2013 Vulcanian explosion at Tungurahua Volcano. Ecuador J Volcanol Geotherm Res 392:106762. https://doi.org/10.1016/j.jvolgeores.2019.106762

Girina OA (2013) Chronology of Bezymianny Volcano activity, 1956–2010. J Volcanol Geotherm Res 263:22–41. https://doi.org/10.1016/j.jvolgeores.2013.05.002

Global Volcanism Program (2021a) Manam. Smithsonian Institution

Global Volcanism Program (2021b) Kadovar. Smithsonian Institution

Global Volcanism Program (2021c) Ulawun. Smithsonian Institution

Hall ML, Steele AL, Bernard B et al (2015) Sequential plug formation, disintegration by Vulcanian explosions, and the generation of granular Pyroclastic Density Currents at Tungurahua volcano (2013–2014), Ecuador. J Volcanol Geotherm Res 306:90–103. https://doi.org/10.1016/j.jvolgeores.2015.09.009

Harris A (2013) Thermal remote sensing of active volcanoes: a user's manual. Cambridge University Press

Harris AJL, Flynn LP, Rothery DA et al (1999) Mass flux measurements at active lava lakes: implications for magma recycling. J Geophys Res Solid Earth 104:7117–7136. https://doi.org/10.1029/98JB02731

Holm RJ, Richards SW (2013) A re-evaluation of arc–continent collision and along-arc variation in the bismarck sea region, Papua New Guinea." Australian Journal of Earth Sciences 60(5):605–19. https://doi.org/10.1080/08120099.2013.824505

James MR, Varley N (2012) Identification of structural controls in an active lava dome with high resolution DEMs: Volcán de Colima, Mexico. Geophys Res Lett 39:. https://doi.org/10.1029/2012GL054245

Jaupart C, Vergniolle S (1988) Laboratory models of Hawaiian and Strombolian eruptions. Nature 331:58–60. https://doi.org/10.1038/331058a0

Johnson JB, Watson LM, Palma JL, Dunham EM, Anderson JF (2018) Forecasting the eruption of an open-vent volcano using resonant infrasound tones. Geophysical Research Letters 45(5):2213–20. https://doi.org/10.1002/2017GL076506

Johnson RW (2013) Fire mountains of the islands: a history of volcanic eruptions and disaster management in Papua New Guinea and the Solomon Islands. ANU E Press

Johnson ER, Wallace PJ, Cashman KV, Delgado Granados H (2010) Degassing of volatiles (H2O, CO2, S, Cl) during ascent, crystallization, and eruption at mafic monogenetic volcanoes in central Mexico. J Volcanol Geotherm Res 197:225–238. https://doi.org/10.1016/j.jvolgeores.2010.02.017

Jugo PJ (2009) Sulfur content at sulfide saturation in oxidized magmas. Geology 37:415–418. https://doi.org/10.1130/G25527A.1

Kazahaya K, Shinohara H, Saito G (1994) Excessive degassing of Izu-Oshima volcano: magma convection in a conduit. Bull Volcanol 56:207–216. https://doi.org/10.1007/BF00279605

Laiolo M, Massimetti F, Cigolini C et al (2018) Long-term eruptive trends from space-based thermal and SO2 emissions: a comparative analysis of Stromboli, Batu Tara and Tinakula volcanoes. Bull Volcanol 80:68. https://doi.org/10.1007/s00445-018-1242-0

Laiolo M, Delle Donne D, Coppola D et al (2022) Shallow magma dynamics at open-vent volcanoes tracked by coupled thermal and SO2 observations. Earth Planet Sci Lett 594:117726. https://doi.org/10.1016/j.epsl.2022.117726

Lev E, Ruprecht P, Oppenheimer C, Peters N, Patrick M, Hernández PA, Spampinato L, Marlow J (2019) A global synthesis of lava lake dynamics. Journal of Volcanology and Geothermal Research 381:16–31. https://doi.org/10.1016/j.jvolgeores.2019.04.010

Lipman PW, Banks NG, Rhodes JM (1985) Degassing-induced crystallization of basaltic magma and effects on lava rheology. Nature 317:604–607. https://doi.org/10.1038/317604a0

Liu EJ, Aiuppa A, Alan A et al (2020) Aerial strategies advance volcanic gas measurements at inaccessible, strongly degassing volcanoes. Sci Adv 6:eabb9103. https://doi.org/10.1126/sciadv.abb9103

Mastin LG, Guffanti M, Servranckx R, Webley P, Barsotti S, Dean K, Durant A, et al. (2009) A multidisciplinary effort to assign realistic source parameters to models of volcanic ash-cloud transport and dispersion during eruptions." Journal of Volcanology and Geothermal Research, Improved Prediction and Tracking of Volcanic Ash Clouds 186(1):10–21. https://doi.org/10.1016/j.jvolgeores.2009.01.008

McCormick BT, Edmonds M, Mather TA et al (2013) Volcano monitoring applications of the Ozone Monitoring Instrument. Geol Soc Lond Spec Publ 380:259–291. https://doi.org/10.1144/SP380.11

McCormick BT, Edmonds M, Mather TA, Carn SA (2012) First synoptic analysis of volcanic degassing in Papua New Guinea. Geochem Geophys Geosystems 13:. https://doi.org/10.1029/2011GC003945

McCormick Kilbride BT, Mulina K, Wadge G et al (2019) Multi-year satellite observations of sulfur dioxide gas emissions and lava extrusion at Bagana Volcano Papua New Guinea. Front Earth Sci 7:9. https://doi.org/10.3389/feart.2019.00009

McCormick Kilbride BT, Nicholson EJ, Wood KT et al (2023) Temporal variability in gas emissions at Bagana Volcano revealed by aerial, ground, and satellite observations. Geochem Geophys Geosystems 24:e2022GC010786. https://doi.org/10.1029/2022GC010786

McKee K, Smith CM, Reath K et al (2021) Evaluating the state-of-the-art in remote volcanic eruption characterization Part II: Ulawun volcano, Papua New Guinea. J Volcanol Geotherm Res 420:107381. https://doi.org/10.1016/j.jvolgeores.2021.107381

McKee CO (1981) Geomorphology, geology and petrology of Manam volcano. Cooke-Ravian Vol Volcanol Pap 23–38
Meerdink SK, Hook SJ, Roberts DA, Abbott EA (2019) The ECOSTRESS spectral library version 1.0. Remote Sens Environ 230:111196. https://doi.org/10.1016/j.rse.2019.05.015
Moussallam Y, Bani P, Curtis A, Barnie T, Moussallam M, Peters N, Schipper CI et al (2016) Sustaining persistent lava Lakes: observations from high-resolution gas measurements at Villarrica Volcano, Chile." Earth and Planetary Science Letters 454: 237–47. https://doi.org/10.1016/j.epsl.2016.09.012
Mueller SB, Varley NR, Kueppers U et al (2013) Quantification of magma ascent rate through rockfall monitoring at the growing/collapsing lava dome of Volcán de Colima, Mexico. Solid Earth 4:201–213. https://doi.org/10.5194/se-4-201-2013
Muth MJ, Wallace PJ (2022) Sulfur recycling in subduction zones and the oxygen fugacity of mafic arc magmas. Earth Planet Sci Lett 599:117836. https://doi.org/10.1016/j.epsl.2022.117836
Palfreyman W, Cooke R (1976) Eruptive history of Manam volcano, Papua New Guinea. Volcanism Australas 201–210
Palma JL, Blake S, Calder ES (2011) Constraints on the rates of degassing and convection in basaltic open-vent volcanoes. Geochem Geophys Geosystems 12:. https://doi.org/10.1029/2011GC003715
Patrick MR, Houghton BF, Anderson KR et al (2020) The cascading origin of the 2018 Kīlauea eruption and implications for future forecasting. Nat Commun 11:5646. https://doi.org/10.1038/s41467-020-19190-1
Patrick M, Anderson KR, Poland MP, Orr TR, Swanson DA (2015) Lava lake level as a gauge of magma reservoir pressure and eruptive hazard. Geology 43(9):831–34. https://doi.org/10.1130/G36896.1
Petrone CM, Mollo S, Gertisser R et al (2022) Magma recharge and mush rejuvenation drive paroxysmal activity at Stromboli volcano. Nat Commun 13:7717. https://doi.org/10.1038/s41467-022-35405-z
Planck M (1901) On the law of distribution of energy in the normal spectrum. Ann Phys 4:1–11
Plank S, Walter TR, Martinis S, Cesca S (2019) Growth and collapse of a littoral lava dome during the 2018/19 eruption of Kadovar Volcano, Papua New Guinea, analyzed by multi-sensor satellite imagery. J Volcanol Geotherm Res 388:106704. https://doi.org/10.1016/j.jvolgeores.2019.106704
Plank S, Walter T, Martinis S, Cesca S (2020) Multi-sensor satellite imagery analysis of the growth and collapse of a littoral lava dome during the 2018/19 eruption of Kadovar Volcano. Papua New Guinea 22:1423
Pyle DM, Mather TA, Biggs J (2013) Remote sensing of volcanoes and volcanic processes: integrating observation and modelling – introduction. Geol Soc Lond Spec Publ 380:1–13. https://doi.org/10.1144/SP380.14
Robin C, Camus G, Gourgaud A (1991) Eruptive and magmatic cycles at Fuego de Colima volcano (Mexico). J Volcanol Geotherm Res 45:209–225. https://doi.org/10.1016/0377-0273(91)90060-D
Rose WI, Palma J, Delgado Granados H, Varley N (2013) Open-vent volcanism and related hazards: overview. Spec Pap Geol Soc Am 498:vii–xiii. https://doi.org/10.1130/2013.2498(00)
Rothery DA, Francis PW, Wood CA (1988) Volcano monitoring using short wavelength infrared data from satellites. J Geophys Res Solid Earth 93:7993–8008. https://doi.org/10.1029/JB093iB07p07993
Shevchenko AV, Dvigalo VN, Walter TR et al (2020) The rebirth and evolution of Bezymianny volcano, Kamchatka after the 1956 sector collapse. Commun Earth Environ 1:1–15. https://doi.org/10.1038/s43247-020-00014-5
Shinohara H (2008) Excess degassing from volcanoes and its role on eruptive and intrusive activity. Rev Geophys 46
Sparks RSJ (1997) Causes and consequences of pressurisation in lava dome eruptions. Earth Planet Sci Lett 150:177–189. https://doi.org/10.1016/S0012-821X(97)00109-X
Sparks RSJ, Biggs J, Neuberg JW (2012) Monitoring volcanoes. Science 335:1310–1311
Stefan J (1879) Uber die Beziehung zwischen der Warmestrahlung und der Temperatur, Sitzungsberichte der mathematisch-naturwissenschaftlichen Classe der kaiserlichen. Akad Wiss 79:S-391
Stix J, Torres RC, Narváez ML et al (1997) A model of Vulcanian eruptions at Galeras volcano, Colombia. J Volcanol Geotherm Res 77:285–303. https://doi.org/10.1016/S0377-0273(96)00100-X
Theys N, Hedelt P, De Smedt I et al (2019) Global monitoring of volcanic SO2 degassing with unprecedented resolution from TROPOMI onboard Sentinel-5 Precursor. Sci Rep 9:2643. https://doi.org/10.1038/s41598-019-39279-y
Vergniolle S, Métrich N (2021) Open-vent volcanoes: a preface to the special issue. Bull Volcanol 83:29. https://doi.org/10.1007/s00445-021-01454-3
Vergniolle S, Métrich N (2022) An interpretative view of open-vent volcanoes. Bull Volcanol 84:83. https://doi.org/10.1007/s00445-022-01581-5
Wilson L (1980) Relationships between pressure, volatile content and ejecta velocity in three types of volcanic explosion. J Volcanol Geotherm Res 8:297–313. https://doi.org/10.1016/0377-0273(80)90110-9
Witter JB, Kress VC, Delmelle P, Stix J (2004) Volatile degassing, petrology, and magma dynamics of the Villarrica Lava Lake, Southern Chile. J Volcanol Geotherm Res 134:303–337. https://doi.org/10.1016/j.jvolgeores.2004.03.002
Woitischek J, Edmonds M, Woods AW (2020) The control of magma crystallinity on the fluctuations in gas composition at open vent basaltic volcanoes. Sci Rep 10:14862. https://doi.org/10.1038/s41598-020-71667-7
Woodhead J, Hergt J, Sandiford M, Johnson W (2010) The big crunch: physical and chemical expressions of arc/continent collision in the Western Bismarck Arc." Journal of Volcanology and Geothermal Research, Making and Breaking the Arc: a volume in honour of Professor John Gamble 190(1):11–24. https://doi.org/10.1016/j.jvolgeores.2009.03.003
Wood M, Foale S, Gabriel J (2019) Anticipating Ulawun Volcano in New Britain. Papua New Guinea. Anthropol Forum 30:30. https://doi.org/10.1080/00664677.2019.1647831
Wooster M, Kaneko T (1998) Satellite thermal analyses of lava dome effusion rates at Unzen Volcano, Japan. J Geophys Res Solid Earth 103:20935–20947
Wooster MJ, Zhukov B, Oertel D (2003) Fire radiative energy for quantitative study of biomass burning: derivation from the BIRD experimental satellite and comparison to MODIS fire products. Remote Sens Environ 86:83–107. https://doi.org/10.1016/S0034-4257(03)00070-1
Wright R (2016) MODVOLC: 14 years of autonomous observations of effusive volcanism from space. Geol Soc Lond Spec Publ 426:23–53. https://doi.org/10.1144/SP426.12
Wright R, Flynn LP, Garbeil H et al (2004) MODVOLC: near-real-time thermal monitoring of global volcanism. J Volcanol Geotherm Res 135:29–49. https://doi.org/10.1016/j.jvolgeores.2003.12.008
Wright R, Blackett M, Hill-Butler C (2015) Some observations regarding the thermal flux from Earth's erupting volcanoes for the period of 2000 to 2014. Geophys Res Lett 42:282–289. https://doi.org/10.1002/2014GL061997
Young S, Voight B, Duffell H (2003) Magma extrusion dynamics revealed by high-frequency gas monitoring at Soufriere Hills Volcano, Montserrat. Geol Soc Lond Spec Publ 213:219–230
Zelenski M, Kamenetsky VS, Nekrylov N, Kontonikas-Charos A (2022) High sulfur in primitive arc magmas, its origin and implications. Minerals 12:37. https://doi.org/10.3390/min12010037